small methods
www.small-methods.com

# Role of Dopants on the Local Electronic Structure of Polymeric Carbon Nitride Photocatalysts

*Jian Ren, Lihua Lin, Klaus Lieutenant, Christian Schulz, Deniz Wong, Thorren Gimm, Annika Bande, Xinchen Wang, and Tristan Petit**

**Polymeric carbon nitride (PCN) is a promising class of materials for solar-to-chemical energy conversion. The increase of the photocatalytic activity of PCN is often achieved by the incorporation of heteroatoms, whose impact on the electronic structure of PCN remains poorly explored. This work reveals that the local electronic structure of PCN is strongly altered by doping with sulfur and iron using X-ray absorption spectroscopy (XAS) and resonant inelastic X-ray scattering (RIXS). From XAS at the carbon and nitrogen K-edges, sulfur atoms are found to mostly affect carbon atoms, in contrast to iron doping mostly altering nitrogen sites. In RIXS at the nitrogen K-edge, a vibrational progression, affected by iron doping, is evidenced, which is attributed to a vibronic coupling between excited electrons in nitrogen atoms and C–N stretching modes in PCN heterocycling rings. This work opens new perspectives for the characterization of vibronic coupling in polymeric photocatalysts.**

## 1. Introduction

Polymeric carbon nitride (PCN) has attracted much attention as a promising metal-free photocatalyst in the past decade.[1] However, the photocatalytic activities of pristine PCN materials remain moderate because of the large optical bandgap, low electric conductivity, and rapid rate of charge-carrier recombination.[2] Optical, electronic, and chemical properties of PCN materials can be influenced by its size, composition, and morphology.[1] Thus, the development of various synthetic methods and modification techniques is highly desirable to optimize PCN photocatalytic properties. Among them, modification of the electronic structure by incorporating heteroatoms into the PCN structure represents an effective approach considering the polymeric nature of PCN and the wide choice of monomers and dopants. Various anions (e.g., B, F, O, P, S, and I) and cations (e.g., K, Fe, Co, Ni, Cu, and Zn) have been introduced into the frameworks of PCN via either interstitial or substitutional doping.[1,3–6] For instance, Fe-doped PCN was reported right after the emergence of PCN photocatalyst as a typical example for the heteroatom modification.[7–11] The Fe—N bonds were homogeneously formed in the PCN matrix during the polycondensation process.[7] An improvement of photooxidation activity was shown in Fe-doped PCN materials, due to the lowering of the bandgap and extension of light absorption in the visible range.[7]

In addition, considering the polymeric nature of PCN, its $\pi$ conjugation can be modified by polymerizing with structure-matching organic comonomers. This also provides another way to introduce heteroatoms into PCN matrix. For example, trithiocyanuric acid has a very similar structure than melamine (MA) that is a common precursor for PCN preparation and can be used to incorporate sulfur atoms into carbon nitrides.[12]

Dr. J. Ren, Dr. T. Petit
Institute for Nanospectroscopy
Helmholtz-Zentrum Berlin für Materialien und Energie GmbH
Albert-Einstein-Straße 15, Berlin 12489, Germany
E-mail: tristan.petit@helmholtz-berlin.de
Dr. J. Ren
Department of Physics
Freie Universität Berlin
Arnimallee 14, Berlin 14195, Germany

The ORCID identification number(s) for the author(s) of this article can be found under https://doi.org/10.1002/smtd.202000707.

© 2020 The Authors. Small Methods published by Wiley-VCH GmbH. This is an open access article under the terms of the Creative Commons Attribution License, which permits use, distribution and reproduction in any medium, provided the original work is properly cited.

[+]Present address: Jülich Centre for Neutron Science JCNS and Peter Grünberg Institut PGI Quantum Materials and Collective Phenomena JCNS-2/PGI-4 Forschungszentrum Jülich GmbH, 52425 Jülich, Germany

Dr. L. Lin, Prof. X. Wang
State Key Laboratory of Photocatalysis on Energy and Environment
College of Chemistry
Fuzhou University
Fuzhou 350002, China
Dr. K. Lieutenant,[+] Dr. C. Schulz, Dr. D. Wong
Department of Methods for Characterization of Transport Phenomena in Energy Materials
Helmholtz-Zentrum Berlin für Materialien und Energie GmbH
Albert-Einstein-Straße 15, Berlin 12489, Germany
T. Gimm
Joint Research Group Simulation of Energy Materials
Helmholtz-Zentrum Berlin für Materialien und Energie GmbH
Hahn-Meitner-Platz 1, Berlin 14109, Germany
Dr. A. Bande
Young Investigator Group Theory of Electron Dynamics and Spectroscopy
Helmholtz-Zentrum Berlin für Materialien und Energie GmbH
Hahn-Meitner-Platz 1, Berlin 14109, Germany

**DOI: 10.1002/smtd.202000707**

The S-doped PCN synthesized through the copolymerization strategy possesses an extended visible light absorption and a high photoreactivity.[13,14]

So far there have been numerous studies on the introduction of various anions and cations into the frameworks of carbon nitrides. Previous studies on doped PCN materials focused on their enhanced photocatalytic performance but the underlying modifications of the electronic structure were rarely explored.[13] To this aim, spectroscopic characterization methods with a high sensitivity to the local chemical structure are highly desired.

X-ray photoelectron spectroscopy (XPS) is often used to probe the binding energy of electronic core levels and obtain information on the chemical bonding of the probed atoms. In addition, synchrotron-based soft X-ray absorption spectroscopy (XAS) can provide further insights into the chemical environment of carbon and nitrogen atoms. XAS probes unoccupied states with element specificity and has been applied to many carbon nanomaterials, including PCN.[15–17] Furthermore, resonant inelastic X-ray scattering (RIXS) data can be obtained when the X-ray photons emitted upon resonant excitation of the unoccupied states identified by XAS are analyzed. RIXS enables probing of the partial density of occupied states with high chemical sensitivity as specific chemical sites are resonantly excited. Over the last years, the development of high-resolution RIXS has enabled the observation of vibrational structures in the quasi-elastic part of RIXS spectra opening new insights into ultrafast molecular dynamics[18] and vibronic coupling in solid materials.[19–22] Nevertheless, RIXS has not been applied to PCN so far to our knowledge.

In this work, PCN materials doped with iron and sulfur atoms are characterized by XAS and RIXS. Each doped sample is compared to pristine PCN samples synthesized under similar conditions. XAS was performed at the C and N K-edges and RIXS at the N K-edge for all the samples. Additionally, XAS and RIXS data at the Fe L-edge were acquired for Fe-PCN. The chemical insights provided by the different spectroscopic techniques are discussed in the following and doping sites for Fe and S atoms in PCN are proposed, supported by density functional theory (DFT) calculations.

## 2. Results and Discussion

### 2.1. Structural Modification and Photocatalytic Activity of Fe- and S-Doped PCN

The pristine and doped PCN samples were prepared according to previously reported methods, which are shortly described in the Experimental Section.[11,12] The doped samples are labeled X-PCN, and the undoped reference samples are referred to as PCN(X), where X represents the heteroatom, i.e., S or Fe, in the following. The structural modification of the PCN upon doping was first characterized by X-ray diffraction (XRD). As shown in Figure S1 in the Supporting Information, PCN(Fe) and PCN(S) possess similar diffraction patterns, in which the main peak located at around 27° corresponds to the layered stacking of heptazine frameworks, while the peak at ≈13° originates from the in-plane repeat period. Incorporation of Fe and S atoms into the PCN framework led to the decreased peak intensities, especially for Fe doping, due to the corrugated layers resulting from the heteroatoms.

From scanning electron microscopy (SEM), the PCN(Fe) prepared by dicyandiamide precursor shows stacking of large particles (Figure S2, Supporting Information). Small particles were formed instead when using melamine as the precursors for PCN(S). Doping PCN with Fe led to much smaller particles than the undoped PCN(Fe). In contrast, thin large-scale sheets were formed with in the case of S doping. The morphology of the PCN samples was further checked by transmission electron microscopy (TEM). Thick particles were observed for PCN(Fe), Fe-PCN, and PCN(S), while PCN(S) shows thin sheet microstructure (Figure S3, Supporting Information), in agreement with the SEM results. From energy dispersive X-ray spectroscopy (EDS), the Fe and S atoms were found to be distributed uniformly across the samples, indicating the homogeneous doping of PCN with Fe and S.

The surface area and porosity of the samples were investigated by $N_2$ adsorption–desorption isotherms. Typical type-IV isotherms with H3-type hysteresis loops were observed for all samples (Figure S4, Supporting Information). The textural parameters are summarized in Table S1 in the Supporting Information, and the results indicate that the surface area of S-PCN is higher than other samples. The pore width distribution determined by the Barrett–Joyner–Halenda method shows the average pore width are around 20 nm for all samples.

The photocatalytic activity of these doped PCN was then assessed to validate the improvement of catalytic activity upon doping. Photocatalytic hydrogen production was used to evaluate the performance of S-doped PCN. As shown in Figure S5 in the Supporting Information, the hydrogen evolution rate of S-PCN was greatly improved in comparison with PCN(S). Incorporating of Fe atoms in PCN framework is favorable for the Fenton reaction, therefore, photocatalytic phenol production from benzene was performed to check the activity of Fe-doped PCN. No measurable conversion was found for the PCN(Fe). In contrast, Fe-PCN shows remarkable phenol production under visible light irradiation (Table S2, Supporting Information). Overall, doping PCN with S and Fe atoms can obviously improve its photocatalytic performance.

### 2.2. XAS at the C and N K-Edges: Modification of PCN Framework upon Doping

The incorporation of dopant atoms can lead to modification of the PCN framework through the (de)formation of chemical bonds with the heteroatoms. The chemical bonding in the doped PCN framework was first studied by XPS and a detailed analysis of the data is available in the Supporting Information. The related modifications of the unoccupied electronic states are monitored by XAS at C and N K-edges. XAS is mostly sensitive to electronic interactions up to 2–3 Å from the probed atom, therefore only the local electronic environment is characterized.[23]

**Figure 1**a displays the C K-edge XA spectra of doped and undoped PCN samples. The XA spectra for undoped PCN(S) and PCN(Fe) are very similar. Three main features are detected in the pre-edge region at ≈285.6 eV (C1), ≈287.8 eV (C2), and ≈288.6 eV (C3). The feature C1 is related to transitions from C 1s electrons to $\pi^*$(C=C), mostly coming from interlayered C=C


© 2020 The Authors. Small Methods published by Wiley-VCH GmbH

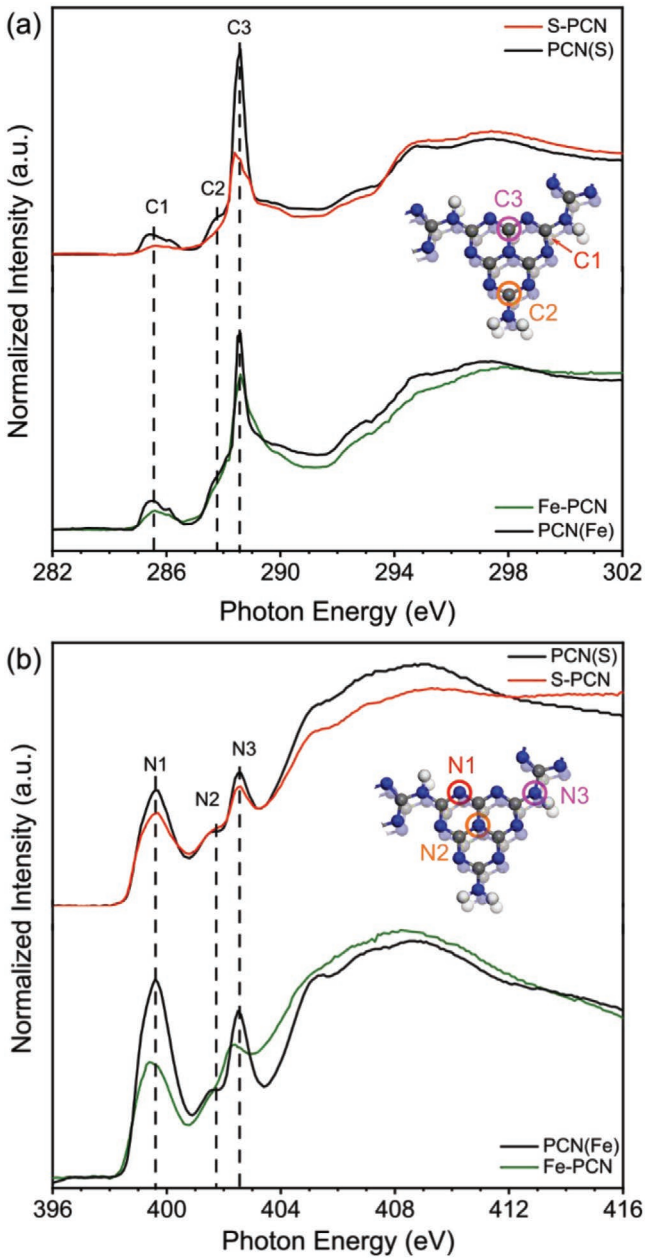


**Figure 1.** XAS study of Fe- and S-doped PCN. XA spectra at a) C K-edge and b) N K-edge of X-PCN and the corresponding reference PCN(X), X = S (red) and Fe (green). The inset shows the simplified PCN structural unit indicating the different species (C: gray; N: blue; H: white) observed in the XA spectra. C1 is targeted to the bonding between two layers. The XA spectra were normalized to the XAS total area.

bonding configuration. C2 represents the excitation of C 1s to $\pi^*$(C–H/C–$NH_2$), related to carbon atoms at the edge of the tri-*s*-triazine structure. C3 is the main XAS contribution associated with transitions to $\pi^*$(N−C=N) from the carbon at the aromatic tri-*s*-triazine structure, which is the basic structural pattern in PCN materials. A small shoulder around ≈289.6 eV is also observed for all samples, which may be related to $\pi^*$(C–N) from defect states in the PCN material. Broad features observed above 292 eV are related to transitions into $\sigma^*$ states.

The introduction of heteroatoms significantly changes the XA spectral features of PCN. In case of sulfur doping, the XA spectrum at the C K-edge is particularly impacted. A drastic decrease of the relative intensity of the C3 feature is observed, associated with the appearance of a shoulder slightly below 289 eV, attributed to defective $sp^3$ C−N bonds. The C2 component is not visible anymore, which is expected since C–$NH_2$ groups were replaced by C–S in the trithiocyanuric acid used as precursor instead of melamine. The C−S bonds are expected at 287.5 eV,[24] where a weak shoulder is visible. Finally, the C1 component is significantly reduced, showing a lower interlayer C=C formation than the reference PCN.

For Fe-PCN, on the other hand, relatively smaller changes at the XAS C K-edge are observed. The intensity of the C3 peak decreases and the peak broadens due to the formation of defective C−N bonds, as also observed by XPS (Figure S8 and Table S3, Supporting Information). Note that the formation of C=O bonds may possibly contribute to the broadening of the C2 feature as a significant oxygen content was detected by XPS for this sample (Figure S6, Supporting Information). Interestingly, the C1 feature is also reduced after Fe doping.

The XA spectra at the N K-edge providing local electronic structures of nitrogen atoms in the different PCN samples are shown in Figure 1b. Three features are found in the pre-edge region at 399.6 eV (N1), 401.7 eV (N2), and 402.6 eV (N3). N1 is assigned to the N 1s →$\pi^*$ transition in aromatic nitrogen atoms of heterocyclic rings, $\pi^*$(C=N−C), N2 to graphitic threefold nitrogen atoms, $\pi^*$(N–3C), and N3 to $sp^3$ N–C bridging among tri-*s*-triazine moieties, $\pi^*$(N–C), respectively.[25,26]

For S-PCN, few changes are observed in the XAS pre-edge region, except a small relative intensity decrease of the N1 and N3 components. For Fe-PCN, the relative decrease of the N1 and N3 peaks is much more pronounced. The N3 feature is shifted to 402.3 eV (–0.3 eV) upon iron doping. This is interpreted by the formation of new C−N−Fe bonds strongly affecting the $\pi^*$(N–C) transitions. As a result, the N2 peak cannot be clearly resolved anymore. The formation of Fe−N bonds in Fe-PCN is confirmed by the appearance of an extra peak at 397.6 eV in the XPS N 1s data (Figure S8 and Table S3, Supporting Information).

From XAS, structural distortion of the tri-*s*-triazine moieties by the incorporation of sulfur or iron atoms into PCN are clearly observed. It appears that the sulfur doping is mostly affecting the chemical environment of the carbon atoms, while the iron doping impacts more significantly the nitrogen sites.

### 2.3. Inelastic Part of the RIXS at the N K-Edge: Modification of Nitrogen-Related Occupied Electronic States

To probe the modifications in the local occupied electronic states in PCN materials upon doping, the partial density of the occupied states of nitrogen atoms was probed using RIXS (**Figure 2**). RIXS enables the investigation of relaxation processes following the incident coherent excitation of unoccupied electronic states.[27–29] Resonant excitation of nitrogen atoms at the different chemical sites in the PCN, identified by XAS, enables the probing of the local occupied electronic states. As the valence band of PCN is mostly populated by N 2p electrons, resonantly exciting the respective atoms may provide further


© 2020 The Authors. Small Methods published by Wiley-VCH GmbH

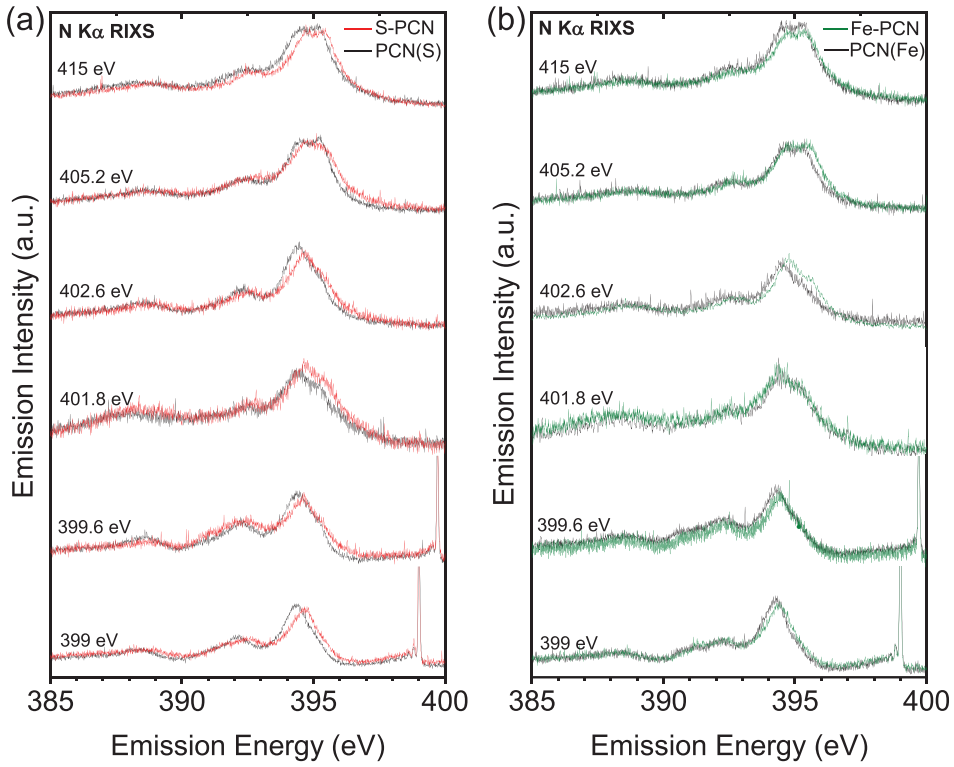


**Figure 2.** RIXS signature of PCN materials at the N K-edge. N K$\alpha$ RIXS spectra of X-PCN and the corresponding reference PCN(X), a) X = S and b) X = Fe.

insights into the modification of the valence band edge usually determined by ultraviolet photoelectron spectroscopy (UPS).

As shown in Figure 2, there are several common features observed in the N K$\alpha$ RIXS spectra: a strong emission centered at 394.5 eV, a small feature located around 392 eV, and a broad band centered at about 388 eV. The emission line at 394.5 eV was assigned to the pyridinic nitrogen in previous work on the carbon nitride thin films,[30] and the emission pattern in Figure 2 is very similar to the previous results observed in polypyridine samples.[31] This main emission peak is already observed at 399 and 399.6 eV excitations, where the N1 nitrogen atom of PCN are excited. All this discussion supports the assignment of the feature at 394.5 eV to pyridinic nitrogen. Note that the broad feature below 389 eV also originates from pyridinic nitrogen.[30] The emission located at 392 eV was previously attributed to $\sigma \rightarrow$1s transitions.[30] This feature splits into two components for excitation energies between 398.6 and 399.0 eV (Figure S10, Supporting Information).

As the excitation energy increases, a new emission line appears at 395.2 eV. This feature can be attributed to the graphitic nitrogen atoms (N2) according to the literature.[25,32] N2 sites are excited by the X-rays at 401.7 eV as determined from XAS therefore this peak only appears in RIXS for higher energy excitation. The other features do not significantly change with the excitation energy because they are mostly related to non-resonant excitation of pyridinic nitrogen sites.

The dispersive features and their line shapes are very similar between doped and undoped PCN samples. The incorporation of heteroatoms leads to a slight upshift (up to +0.3 eV) of the main emission peaks position around 395 eV associated to pyridinic and graphitic nitrogen atoms. The higher emission intensity in this region may result from a charge transfer toward the nitrogen atoms.[33] For both doped samples, the valence band edge measured by UPS is raised compared to that of pristine samples (Figure S9, Supporting Information). As a result, the bandgap of the PCN materials is reduced to –0.2 and –0.3 eV for S- and Fe-doped PCN, respectively. Indeed, the energy onset on the XAS, corresponding to the conduction band minimum, does not seem to be strongly affected by the doping. The valence band upshift is probably related to the shift of the occupied electronic states related to nitrogen atoms upon sulfur and iron doping.

### 2.4. Quasi-Elastic Part of the RIXS at the N K-Edge: Vibronic Coupling in PCN

In the energy region close to the elastic line, a clear vibration progression in the RIXS spectra is observed as shown in **Figure 3**. Note that the RIXS spectra are shown in energy loss scale to better identify the loss features. Each vibrational peak is symmetric and was fitted by Gaussian profile with a fixed energy width that represents its vibrational energy. Up to four harmonics separated by a frequency of 190 meV are resolved for all the samples characterized at room temperature. No clear energy dependent variation was observed within the range 398.2–399.4 eV, except a relative decrease of the RIXS signal for large detuning (Figures S10 and S11, Supporting Information). These vibrational modes disappear above 399.6 eV excitation.

The well-resolved vibrational progression demonstrates a significant coupling between the excited electrons in the C=N–C


© 2020 The Authors. Small Methods published by Wiley-VCH GmbH

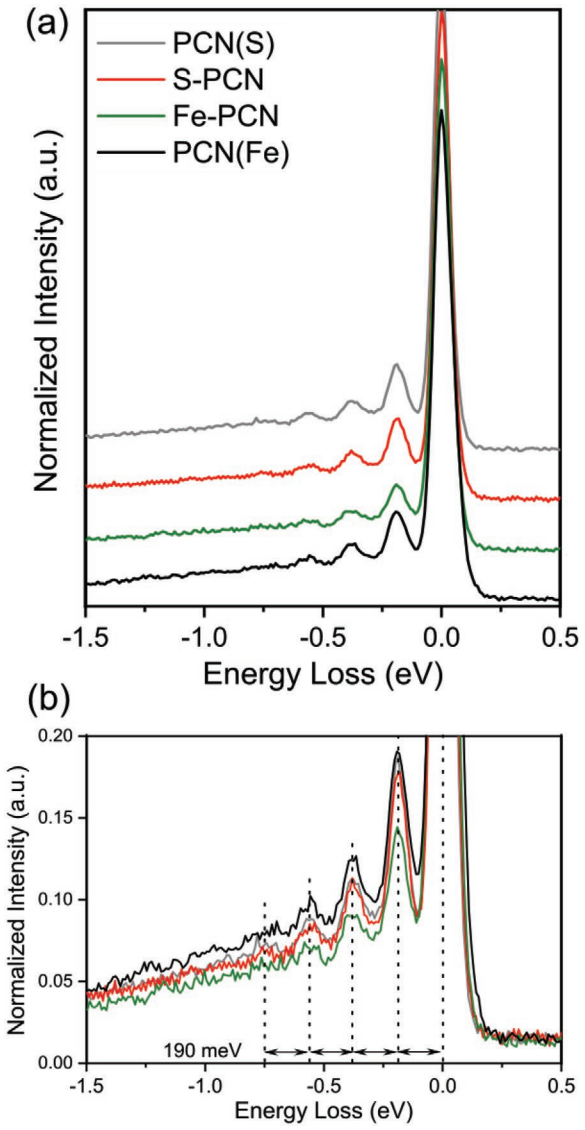


**Figure 3.** Quasi-elastic RIXS signature of PCN materials at the N K-edge. a) Energy loss feature detected from N K$\alpha$ RIXS obtained after excitation at 399 eV. Zero energy loss ($E$ = 0 eV) corresponds to the elastic line. b) The vibrational progression is highlighted. All spectra were normalized to the maximum of the elastic line.

sites of the heterocyclic rings and C–N stretching modes. During the motion of the excited electrons, the potential energy surface of the core-excited state varies and may overlap with ground vibrational levels, which leads to the vibrational progression observed in the RIXS spectrum.[34] In general, the intensity and the number of vibrational progression depends on the overlap of the vibrational wave function in the ground and excited states. The loss of the vibrational features for excitation above 399.6 eV is related to a quenching of the vibronic coupling for detuned excitation energy.[35]

Electron–phonon coupling has been estimated from experimental RIXS data on strongly correlated materials using the Ament model when the time scale of the phonon mode is much shorter than the core-hole lifetime.[19–21] In our case, the CN stretching mode (190 meV, corresponding to ≈22 fs) is slightly larger than the core-hole lifetime broadening at the N 1s (100–130 meV, ≈30–40 fs)[36,37] therefore this procedure cannot be applied.[22] Furthermore, Geondzhian and Gilmore recently suggested that RIXS may rather be probing exciton–phonon coupling when the core-hole is not well screened,[38] which is likely to be the case for PCN. In particular, optical excitons have a high binding energy in PCN materials[39] and were found to play a significant role in their photoactivity.[40] Further work on the theoretical description of RIXS process in PCN would be required to extract quantitative information from these experimental data.

Nevertheless, qualitative insights on vibronic coupling can still be obtained from the comparison of the different samples. The frequency of the vibrational modes remains constant after heteroatom doping, showing that the local structure of the PCN close to the C=N–C bonds is not significantly affected. On the other hand, the intensity of the vibrational modes decreases slightly after Fe doping, which is not observed for S-doped sample. Fe doping is therefore reducing the vibronic coupling between the excited electron in the nitrogen site and the CN stretching mode. Ivanov et al. proposed that a strong vibronic coupling between unoccupied and occupied molecular orbitals would induce a buckling of the PCN planes,[41] which would be suppressed by doping with cations lying between tri-*s*-triazine groups. We might interpret the relative intensity decrease of vibrational progression for Fe-PCN by a quenching of the vibronic coupling induced by Fe atoms at similar doping sites. This result agrees with the XAS observation that Fe doping mostly affects nitrogen sites while S doping has rather an impact on carbon atoms. This is also supported by DFT calculations as discussed in Section 2.6.

The RIXS spectra can be compared to vibrational spectroscopy measurements. For PCN materials, the energy separation of the vibrational progressions shown in the N K$\alpha$ RIXS spectra is 190 meV corresponding to the C–N stretching peak at 1532–1540 $cm^{-1}$ usually observed by IR or Raman spectroscopy. Taking PCN(S) as an example, a band at 1538 $cm^{-1}$ is found in the IR spectrum (Figure S12, Supporting Information). Since the RIXS measurement is performed at the resonant excitation of the N1 feature (Figure 2b), this IR vibration band can be attributed to the C=N–C bonds in the aromatic rings. Due to the symmetry selection rule for the RIXS process,[42,43] other C–N vibrations are not visible by RIXS. The high element- and site-selectivity of RIXS enables the identification of the molecular vibronic structure, which cannot be achieved with classical vibrational spectroscopies. It is noteworthy that vibronic coupling was previously evidenced by RIXS at the N K-edge in aqueous ammonia,[44] spin-liquid insulator,[22] and on small organic molecules with other vibrational modes.[45,46] Our work demonstrates that RIXS can also be used to probe vibronic interactions in polymeric material.

### 2.5. XAS and RIXS at the Fe L-Edge: Electronic Interaction of Fe in PCN

The XAS at the Fe L-edge, shown in **Figure 4**a, has a typical signature of Fe species in the oxidation state +3, with an $L_3$-edge


© 2020 The Authors. Small Methods published by Wiley-VCH GmbH

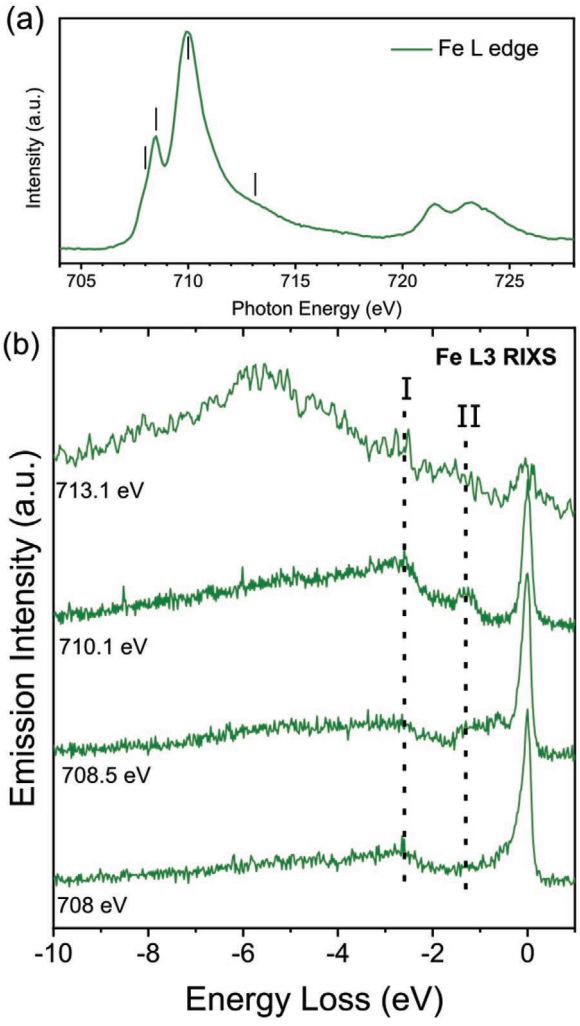


**Figure 4.** XAS and RIXS of iron dopant in Fe-PCN. a) XAS at the Fe L-edge for Fe-PCN. b) Energy loss feature detected from Fe $L_3$ RIXS. Zero energy loss ($E = 0$ eV) corresponds to the elastic line. The excitation energies for the RIXS are labeled as black lines in (a).

composed of two peaks resulting from ligand field effects. The shoulder at 713.1 eV may be related to a charge transfer state resulting from the hybridization with oxygen atoms,[47] which was clearly observed for this sample, and possibly nitrogen atoms. The Fe $L_3$-edge RIXS of Fe-PCN (Figure 4b) was also recorded at selected photon energies corresponding to the main X-ray absorption features and is plotted as a function of the energy loss to better recognize constant energy-loss features. At the resonant excitations, pronounced features below the elastic line can be observed. In addition to the elastic peak, two energy loss features at −2.6 eV (I) and −1.3 eV (II), attributed to d–d excitations, can be observed.[47,48] Peak II is very weak at 708 eV excitation energy, but is clearly observed with the other three incident excitation energies. These features, with an energy lying in the visible range, may explain the extended optical absorption observed for Fe-doped PCN.[10] When the incident energy is detuned above the $L_3$ resonance (713.1 eV), a broad band around −5.6 eV (707.4 eV) is observed, which is related to transitions from 3d to 2p states localized at the Fe atom.[49] This peak is not observed for excitations at lower energies. At this stage, the impact of the interaction with the PCN matrix on iron electronic structure remains unclear. Nevertheless, the confirmation of $Fe^{3+}$ ions in the PCN may contribute to explain the higher photocatalytic activity of Fe-doped PCN for phenol production from benzene. $Fe^{3+}$ ions can trap the photogenerated electrons, which can reduce $O_2$ to "$\bullet O_2^-$."[10] Meanwhile, $Fe^{3+}$ ion can serve as a mediator to facilitate the oxidation of $OH^-$ and $H_2O$ molecules to "•OH" by valence holes.[8]

### 2.6. Possible Fe and S Doping Sites on PCN

Based on these X-ray spectroscopic data, possible doping sites can be suggested, which should be validated by theoretical calculations. The possible structures of undoped and doped PCN were optimized using DFT and the optimal structures are shown in **Figure 5**. The undoped PCN trimer (Figure 5a) is nearly planar with a buckling distortion in the center, as previously observed by Ivanov et al.[41] This distortion is due to a pseudo Jahn–Teller effect arising from couplings between the occupied and unoccupied molecular orbitals of the molecule.[41] Upon addition of sulfur the structure is locally distorted due to the larger size of the S atom but the overall structure stays intact (Figure 5b). Two configurations were considered, namely, with sulfur replacing the carbon or nitrogen atoms. While Hong et al.[14] suggested the sulfur to replace only carbon atoms, both carbon- and nitrogen-substituted structures were found to be stable. Based on the previous discussion, it is more likely that sulfur atoms replace nitrogen atoms into the PCN structure. Thereby, it would induce strong distortions of the local chemical environment of C3 atoms but minimally affects N atoms.

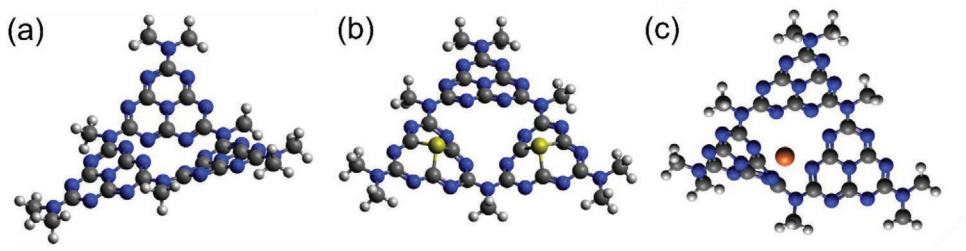


**Figure 5.** DFT-optimized PCN trimer structure for a) undoped trimer, b) S-PCN and c) Fe-PCN with proposed doping sites. The following colors were used: C: gray; N: blue; H: white; S: yellow; Fe: orange.


© 2020 The Authors. Small Methods published by Wiley-VCH GmbH

For the Fe-doped PCN trimer a different picture is obtained. Geometry optimization of an iron atom placed in the exact center of the trimer does not yield a stable structure. Instead, the metal atom locates favorably near one of the tri-*s*-triazine units, which leads to a major deformation of the surrounding structure. In the equilibrium structure shown in Figure 5c, the nearby part of the tri-*s*-triazine unit is bent toward the iron atom, thereby providing coordination with nitrogen atoms from additional directions. Iron naturally prefers octahedral coordination, which cannot be provided by a near-planar structure and thus induces substantial structural change. In their study on iron doping of hetero-layered g-$C_3N_4$ and graphene nanomeshes, Wang et al.[50] pointed out that the iron will most likely be coordinated between two layers of the material. This can equally be expected for the PCN polymer structures. Nonetheless, substantial structural deformation will occur due to the strong coordination effects of iron.

The structural features described above are well in line with the experimental results on the quasi-elastic RIXS structures at the N K-edge. The minor structural changes that occur upon S doping explain why the vibrational progression found in the RIXS N K-edge spectra is mainly preserved. On the other hand, Fe doping introduces major structural changes, which become visible in the change of the RIXS vibrational fine structure.

## 3. Conclusion

In this work, the influence of doping with sulfur and iron atoms on PCN materials is investigated by soft X-ray spectroscopies. Clear modifications of the electronic structure are detected for both dopants. The local structures of unoccupied and occupied states were characterized using XAS and RIXS, respectively. While sulfur atoms are mostly affecting carbon sites, the iron doping has a stronger impact on the nitrogen sites. Furthermore, vibronic coupling between excited electrons and C–N stretching modes were evidenced in PCN materials using RIXS. It is impacted by iron doping but not by sulfur doping. Based on the X-ray spectroscopic data and supported by DFT calculations, different doping sites are suggested for Fe and S atoms. This study highlights that high-resolution RIXS opens new perspective for the understanding of local electronic and vibronic interactions in the emerging organic photocatalytic polymeric materials. Correlating these properties with the photocatalytic activity of PCN materials may facilitate the rational design of more efficient PCN photocatalysts in the future.

## 4. Experimental Section

*Sample Preparation*: The samples were prepared according to previously reported methods.[11,12] MA and dicyandiamide (DCDA) were used as the precursors to prepare PCN(S) and PCN(Fe), respectively. Typically, 2 g MA (or DCDA) was loaded into a 50 mL crucible with cover. The precursor was heated to 600 °C for 4 h with the ramp rate of 6 °C $min^{-1}$ under $N_2$ atmosphere (250 mL $min^{-1}$). After naturally cooling down, the bulk sample was ground into powder by agate mortar for further use. The preparation procedure of S-doped PCN (S-PCN) was the same as PCN(S) but trithiocyanuric acid was used as the precursor. For the Fe-doped PCN (Fe-PCN), 1 g DCDA was dispersed in 5 mL deionized water by sonication. Then, the solution was stirred and 0.1 g $FeCl_3$ was added to the solution. The mixed solution was heated at 100 °C with continuous stirring to remove water. Finally, the as-obtained mixture was used as the precursor to prepare Fe-PCN following the same synthetic procedure of PCN(Fe).

XRD measurements were carried out on a Bruker D8 Advance diffractometer with Cu-K$\alpha$1 radiation ($\lambda$ = 1.5406 Å). The morphology of the samples was investigated by the HITACHI SU8010 field emission SEM. TEM, elemental mapping, and EDS were performed on a FEI Tencai 20 microscope. The $N_2$ adsorption–desorption isotherms were collected at 77 K using a Micromeritics ASAP 2460 surface area and porosity analyzer.

*Photocatalytic Activity*: Photocatalytic hydrogen production was performed in a Pyrex top-irradiation reaction vessel connected to a glass closed gas system. Photocatalyst (50 mg) was added in an aqueous solution (100 mL) containing 10 mL of triethanolamine (TEOA) as electron donor. Pt (3 wt%) was loaded on the surface of the photocatalyst as the cocatalyst using an in situ photodeposition method with $H_2PtCl_6$ as precursor. The reaction solution was evacuated several times to remove air prior to the irradiation using a 300 W Xe lamp. The wavelength of the incident light was controlled by applying appropriate long-pass cut-off filters ($\lambda > 420$ nm). The temperature of the reaction solution was maintained at room temperature using a flow of cooling water during the reaction. The evolved gases were determined by a gas chromatography equipped with a thermal conductive detector (TCD) and a 5 Å molecular sieve column, using Ar as the carrier gas.

For the photocatalytic phenol production from benzene, photocatalyst (50 mg) was milled and then suspended in a mixture of acetonitrile (4 mL), benzene (0.8 mL, 9 mmol), water (4 mL), and $H_2O_2$ (30 wt%, 0.51 mL, 5 mmol). The resulting biphasic system was stirred at 60 °C for 4 h. A 300 W Xenon lamp equipping with a 420 nm cut-off filter was used as the visible light source for the irradiation of reaction system. At the end of the reaction, ethanol (5 mL) was poured into the mixture at 4 °C for quenching the reaction and to turn the biphasic system to a single-phase one. The products of the reactions were analyzed by a gas chromatograph (HP6890) and GC-MS with toluene as the internal standard.

*X-Ray Absorption Spectroscopy*: The XA spectra were acquired in total electron yield (TEY) mode on the PCN material drop cast on a conductive Si substrate. The measurements were performed at the U49/2 PGM-1 beamline of the synchrotron BESSY II using the LiXEdrom endstation. For the C K-edge (N K-edge), the spectra were normalized to the XAS area calculated over the region 280–310 eV (396–420 eV).

*Resonant Inelastic X-Ray Scattering*: The RIXS measurements were performed at the U41-PEAXIS beamline using the endstation PEAXIS of BESSY II.[51] The samples were prepared using the same procedure as for XAS. The RIXS spectra were acquired with an incident angle on the sample of 65° and a scattering angle 2$\theta$ of 130°. The instrument resolution was optimized to 85 meV at the N K-edge using a tape and about 195 meV at the Fe L-edge. Each spectrum measured at the N K-edge was acquired for 10 min and accumulated to a total of 1 h of measurements, whereas the Fe L-edge spectra were acquired for 5 min to a total of 30 min per incident energy.

*Theoretical Methods*: Ground-state structures of doped and undoped PCN structures were calculated within the DFT framework using the ORCA program suite.[52,53] The choice of DFT functionals was aided by the detailed study of Goerigk and Grimme.[54] The structures were preoptimized using the revPBE GGA functional[55] and Ahlrich's triple-zeta def2-TZVP basis set.[56,57] Numerical frequency analysis was performed to confirm that the global structural minimum was reached. The molecules were subsequently further optimized with the more accurate PW6B95 hybrid functional[58] and the same basis set, but no significant differences in structures were observed. All structure optimizations employed Grimme's third order atom-pairwise dispersion correction with Becke–Jones (D3BJ) dampening.[59] The RIJCOSX approximation[60] together with the appropriate def2-TVP/J auxiliary basis sets[61] was used to speed up integral calculation.

The undoped PCN structure consists of a closed trimer with sum formula $C_{27}N_{27}H_{27}$ as shown in Figure 5. The same model was already


© 2020 The Authors. Small Methods published by Wiley-VCH GmbH

suggested by Hong et al.[14] who studied effects of sulfur doping on PCN. Two carbon atoms or two nitrogen atoms are replaced by sulfur, respectively, to obtain two different S-doped structures. A single iron atom is placed in the center of the structure to obtain Fe-doped PCN.[41,50] The PCN structures were plotted using Avogadro software.

## Supporting Information

Supporting Information is available from the Wiley Online Library or from the author.

## Acknowledgements

This work was financially supported by the Volkswagen Foundation (Freigeist Fellowship No. 89592) and the National Natural Science Foundation of China (Grant Nos. U1905214 and 21961142019). T.G. was funded by the HEIBRiDS Graduate School. The help with XPS from Iver Lauermann and with FTIR from Ulrich Schade is acknowledged. The authors acknowledge the kind support from the staff of the BESSY II synchrotron facility, especially Ronny Golnak and Jie Xiao. The authors thank the Helmholtz-Zentrum Berlin for the allocation of beamtime at the U49/2 PGM-1 and U41-PEAXIS synchrotron beamlines at BESSY II.

Open access funding enabled and organized by Projekt DEAL.

## Conflict of Interest

The authors declare no conflict of interest.

## Keywords

doping, polymeric carbon nitride, resonant inelastic X-ray scattering, vibronic coupling, X-ray absorption spectroscopy

Received: August 10, 2020
Revised: October 2, 2020
Published online: November 3, 2020

[1] F. K. Kessler, Y. Zheng, D. Schwarz, C. Merschjann, W. Schnick, X. Wang, M. J. Bojdys, *Nat. Rev. Mater.* **2017**, *2*, 17030.
[2] Y. Zheng, L. Lin, B. Wang, X. Wang, *Angew. Chem., Int. Ed.* **2015**, *54*, 12868.
[3] H. Wang, L. Zhang, Z. Chen, J. Hu, S. Li, Z. Wang, J. Liu, X. Wang, *Chem. Soc. Rev.* **2014**, *43*, 5234.
[4] L. Jiang, X. Yuan, Y. Pan, J. Liang, G. Zeng, Z. Wu, H. Wang, *Appl. Catal., B* **2017**, *217*, 388.
[5] X. Liu, R. Ma, L. Zhuang, B. Hu, J. Chen, X. Liu, X. Wang, *Crit. Rev. Environ. Sci. Technol.* **2020**, https://doi.org/10.1080/10643389.2020.1734433.
[6] V. Hasija, P. Raizada, A. Sudhaik, K. Sharma, A. Kumar, P. Singh, S. B. Jonnalagadda, V. K. Thakur, *Appl. Mater.* **2019**, *15*, 494.
[7] X. Wang, X. Chen, A. Thomas, X. Fu, M. Antonietti, *Adv. Mater.* **2009**, *21*, 1609.
[8] Y. Li, S. Ouyang, H. Xu, X. Wang, Y. Bi, Y. Zhang, J. Ye, *J. Am. Chem. Soc.* **2016**, *138*, 13289.
[9] L.-F. Gao, T. Wen, J.-Y. Xu, X.-P. Zhai, M. Zhao, G.-W. Hu, P. Chen, Q. Wang, H.-L. Zhang, *ACS Appl. Mater. Interfaces* **2016**, *8*, 617.
[10] S. Tonda, S. Kumar, S. Kandula, V. Shanker, *J. Mater. Chem. A* **2014**, *2*, 6772.
[11] X. Chen, J. Zhang, X. Fu, M. Antonietti, X. Wang, *J. Am. Chem. Soc.* **2009**, *131*, 11658.
[12] J. Zhang, J. Sun, K. Maeda, K. Domen, P. Liu, M. Antonietti, X. Fu, X. Wang, *Energy Environ. Sci.* **2011**, *4*, 675.
[13] G. Liu, P. Niu, C. Sun, S. C. Smith, Z. Chen, G. Q. (Max) Lu, H.-M. Cheng, *J. Am. Chem. Soc.* **2010**, *132*, 11642.
[14] J. Hong, X. Xia, Y. Wang, R. Xu, *J. Mater. Chem.* **2012**, *22*, 15006.
[15] J.-R. Zhang, Y. Ma, S.-Y. Wang, J. Ding, B. Gao, E. Kan, W. Hua, *Phys. Chem. Chem. Phys.* **2019**, *21*, 22819.
[16] N. Meng, J. Ren, Y. Liu, Y. Huang, T. Petit, B. Zhang, *Energy Environ. Sci.* **2018**, *11*, 566.
[17] Y. Li, J. Ren, S. Ouyang, W. Hou, T. Petit, H. Song, H. Chen, D. Philo, T. Kako, J. Ye, *Appl. Catal., B* **2019**, *259*, 118027.
[18] F. Hennies, A. Pietzsch, M. Berglund, A. Föhlisch, T. Schmitt, V. Strocov, H. O. Karlsson, J. Andersson, J.-E. Rubensson, *Phys. Rev. Lett.* **2010**, *104*, 193002.
[19] L. J. P. Ament, M. van Veenendaal, J. van den Brink, *EPL* **2011**, *95*, 27008.
[20] J. G. Vale, C. D. Dashwood, E. Paris, L. S. I. Veiga, M. Garcia-Fernandez, A. Nag, A. Walters, K.-J. Zhou, I.-M. Pietsch, A. Jesche, P. Gegenwart, R. Coldea, T. Schmitt, D. F. McMorrow, *Phys. Rev. B* **2019**, *100*, 224303.
[21] D. Meyers, K. Nakatsukasa, S. Mu, L. Hao, J. Yang, Y. Cao, G. Fabbris, H. Miao, J. Pelliciari, D. McNally, M. Dantz, E. Paris, E. Karapetrova, Y. Choi, D. Haskel, P. Shafer, E. Arenholz, T. Schmitt, T. Berlijn, S. Johnston, J. Liu, M. P. M. Dean, *Phys. Rev. Lett.* **2018**, *121*, 236802.
[22] V. Ilakovac, S. Carniato, P. Foury-Leylekian, S. Tomić, J.-P. Pouget, P. Lazić, Y. Joly, K. Miyagawa, K. Kanoda, A. Nicolaou, *Phys. Rev. B* **2017**, *96*, 184303.
[23] F. Weber, J. Ren, T. Petit, A. Bande, *Phys. Chem. Chem. Phys.* **2019**, *21*, 6999.
[24] J. Stöhr, J. L. Gland, E. B. Kollin, R. J. Koestner, A. L. Johnson, E. L. Muetterties, F. Sette, *Phys. Rev. Lett.* **1984**, *53*, 2161.
[25] W. T. Zheng, J. H. Guo, Y. Sakamoto, M. Takaya, X. T. Li, P. J. Chao, Z. S. Jin, K. Z. Xing, J.-E. Sundgren, *Diamond Relat. Mater.* **2001**, *10*, 1897.
[26] S. C. Ray, C. W. Pao, J. W. Chiou, H. M. Tsai, J. C. Jan, W. F. Pong, R. McCann, S. S. Roy, P. Papakonstantinou, J. A. McLaughlin, *J. Appl. Phys.* **2005**, *98*, 033708.
[27] L. Zhang, N. Schwertfager, T. Cheiwchanchamnangij, X. Lin, P.-A. Glans-Suzuki, L. F. J. Piper, S. Limpijumnong, Y. Luo, J. F. Zhu, W. R. L. Lambrecht, J.-H. Guo, *Phys. Rev. B* **2012**, *86*, 245430.
[28] L. J. P. Ament, M. van Veenendaal, T. P. Devereaux, J. P. Hill, J. van den Brink, *Rev. Mod. Phys.* **2011**, *83*, 705.
[29] J. A. Carlisle, E. L. Shirley, E. A. Hudson, L. J. Terminello, T. A. Callcott, J. J. Jia, D. L. Ederer, R. C. C. Perera, F. J. Himpsel, *Phys. Rev. Lett.* **1995**, *74*, 1234.
[30] N. Hellgren, J. Guo, Y. Luo, C. Såthe, A. Agui, S. Kashtanov, J. Nordgren, H. Ågren, J.-E. Sundgren, *Thin Solid Films* **2005**, *471*, 19.
[31] M. Magnuson, L. Yang, J.-H. Guo, C. Såthe, A. Agui, J. Nordgren, Y. Luo, H. Ågren, N. Johansson, W. R. Salaneck, L. E. Horsburgh, A. P. Monkman, *J. Electron Spectrosc. Relat. Phenom.* **1999**, *101–103*, 573.
[32] C.-H. Chuang, S. C. Ray, D. Mazumder, S. Sharma, A. Ganguly, P. Papakonstantinou, J.-W. Chiou, H.-M. Tsai, H.-W. Shiu, C.-H. Chen, H.-J. Lin, J. Guo, W.-F. Pong, *Sci. Rep.* **2017**, *7*, 42235.
[33] N. Engel, S. I. Bokarev, E. Suljoti, R. Garcia-Diez, K. M. Lange, K. Atak, R. Golnak, A. Kothe, M. Dantz, O. Kühn, E. F. Aziz, *J. Phys. Chem. B* **2014**, *118*, 1555.
[34] S. Schreck, A. Pietzsch, B. Kennedy, C. Såthe, P. S. Miedema, S. Techert, V. N. Strocov, T. Schmitt, F. Hennies, J.-E. Rubensson, A. Föhlisch, *Sci. Rep.* **2016**, *6*, 20054.
[35] P. Skytt, P. Glans, J.-H. Guo, K. Gunnelin, C. Såthe, J. Nordgren, F. K. Gel'mukhanov, A. Cesar, H. Ågren, *Phys. Rev. Lett.* **1996**, *77*, 5035.
[36] M. Neeb, J.-E. Rubensson, M. Biermann, W. Eberhardt, *J. Electron Spectrosc. Relat. Phenom.* **1994**, *67*, 261.


© 2020 The Authors. Small Methods published by Wiley-VCH GmbH

[37] B. Kempgens, A. Kivimäki, M. Neeb, H. M. Köppe, A. M. Bradshaw, J. Feldhaus, *J. Phys. B: At., Mol. Opt. Phys.* **1996**, *29*, 5389.
[38] A. Geondzhian, K. Gilmore, *Phys. Rev. B* **2018**, *98*, 214305.
[39] S. Melissen, T. Le Bahers, S. N. Steinmann, P. Sautet, *J. Phys. Chem. C* **2015**, *119*, 25188.
[40] Y. Li, S. Jin, X. Xu, H. Wang, X. Zhang, *J. Appl. Phys.* **2020**, *127*, 170903.
[41] A. S. Ivanov, E. Miller, A. I. Boldyrev, Y. Kameoka, T. Sato, K. Tanaka, *J. Phys. Chem. C* **2015**, *119*, 12008.
[42] R. C. Couto, V. V. Cruz, E. Ertan, S. Eckert, M. Fondell, M. Dantz, B. Kennedy, T. Schmitt, A. Pietzsch, F. F. Guimarães, H. Ågren, F. Gel'mukhanov, M. Odelius, V. Kimberg, A. Föhlisch, *Nat. Commun.* **2017**, *8*, 14165.
[43] V. Vaz da Cruz, E. Ertan, R. C. Couto, S. Eckert, M. Fondell, M. Dantz, B. Kennedy, T. Schmitt, A. Pietzsch, F. F. Guimarães, H. Ågren, F. Gel'mukhanov, M. Odelius, A. Föhlisch, V. Kimberg, *Phys. Chem. Chem. Phys.* **2017**, *19*, 19573.
[44] L. Weinhardt, M. Weigand, O. Fuchs, M. Bär, M. Blum, J. D. Denlinger, W. Yang, E. Umbach, C. Heske, *Phys. Rev. B* **2011**, *84*, 104202.
[45] J. N. O'Shea, K. Handrup, R. H. Temperton, A. J. Gibson, A. Nicolaou, N. Jaouen, *J. Chem. Phys.* **2017**, *147*, 134705.
[46] R. H. Temperton, S. T. Skowron, K. Handrup, A. J. Gibson, A. Nicolaou, N. Jaouen, E. Besley, J. N. O'Shea, *J. Chem. Phys.* **2019**, *151*, 074701.
[47] J. Miyawaki, S. Suga, H. Fujiwara, M. Urasaki, H. Ikeno, H. Niwa, H. Kiuchi, Y. Harada, *Phys. Rev. B* **2017**, *96*, 214420.
[48] L.-C. Duda, J. Nordgren, G. Dräger, S. Bocharov, T. Kirchner, *J. Electron Spectrosc. Relat. Phenom.* **2000**, *110–111*, 275.
[49] K. Atak, S. I. Bokarev, M. Gotz, R. Golnak, K. M. Lange, N. Engel, M. Dantz, E. Suljoti, O. Kühn, E. F. Aziz, *J. Phys. Chem. B* **2013**, *117*, 12613.
[50] C. Wang, H. Zhao, J. Wang, Z. Zhao, M. Cheng, X. Duan, Q. Zhang, J. Wang, J. Wang, *J. Mater. Chem. A* **2019**, *7*, 1451.
[51] C. Schulz, K. Lieutenant, J. Xiao, T. Hofmann, D. Wong, K. Habicht, *J. Synchrotron Radiat.* **2020**, *27*, 238.
[52] F. Neese, *Wiley Interdiscip. Rev.: Comput. Mol. Sci.* **2018**, *8*, e1327.
[53] F. Neese, F. Wennmohs, U. Becker, C. Riplinger, *J. Chem. Phys.* **2020**, *152*, 224108.
[54] L. Goerigk, S. Grimme, *Phys. Chem. Chem. Phys.* **2011**, *13*, 6670.
[55] Y. Zhang, W. Yang, *Phys. Rev. Lett.* **1998**, *80*, 890.
[56] A. Schäfer, H. Horn, R. Ahlrichs, *J. Chem. Phys.* **1992**, *97*, 2571.
[57] F. Weigend, R. Ahlrichs, *Phys. Chem. Chem. Phys.* **2005**, *7*, 3297.
[58] Y. Zhao, D. G. Truhlar, *J. Phys. Chem. A* **2005**, *109*, 5656.
[59] S. Grimme, S. Ehrlich, L. Goerigk, *J. Comput. Chem.* **2011**, *32*, 1456.
[60] F. Neese, F. Wennmohs, A. Hansen, U. Becker, *Chem. Phys.* **2009**, *356*, 98.
[61] F. Weigend, *Phys. Chem. Chem. Phys.* **2006**, *8*, 1057.


© 2020 The Authors. Small Methods published by Wiley-VCH GmbH